International Journal of Nanomedicine

Dovepress
Taylor & Francis Group

Open Access Full Text Article

ORIGINAL RESEARCH

Evaluation of Self-Regulating Doped Ferrite Nanoparticles with Glucose, Chitosan, and Poly-Ethylene Glycol Coatings for Hyperthermia and Dual Imaging

Alessandro Negri[1], Anita Conti[1], Emil Milan[2], Enrico Forlin[3], Filippo Gherlinzoni[4], Giovanni Morana[4], Michele Gottardi[4], Paolo Matteazzi[3,4], Adolfo Speghini[2,5], Andre Bongers[6], Pasquina Marzola[1,5]

[1]Department of Engineering for Innovation Medicine, University of Verona, Verona, Italy; [2]Nanomaterials Research Group, Department of Biotechnology, University of Verona, Verona, Italy; [3]M.B.N. Nanomaterialia S.p.A., Carbonera, Treviso, Italy; [4]Foundation for Nanotheranostics Research in Cancer Therapy, Treviso, Italy; [5]National Interuniversity Consortium of Materials Science and Technology, Firenze, Italy; [6]Biological Resources Imaging Laboratory, Mark Wainwright Analytical Centre, UNSW Sydney, Sydney, NSW, Australia

Correspondence: Pasquina Marzola, Department of Engineering for Innovation Medicine, University of Verona, Strada le Grazie – 15, Verona, 37134, Italy, Email pasquina.marzola@univr.it

Purpose: This study investigates the theranostic potential of doped ferrite nanoparticles (NPs) with self-regulating temperature (SRT) properties, termed M55, coated with glucose (GM55), chitosan (CM55), and poly-ethylene glycol (PM55). The NPs were assessed for their physicochemical attributes, magnetic fluid hyperthermia (MFH) efficacy, dual-imaging capabilities in Magnetic Resonance Imaging (MRI) and Magnetic Particle Imaging (MPI), cytocompatibility, and cellular uptake.

Methods: Physicochemical characterization was conducted using Fourier-transform infrared spectroscopy (FTIR), dynamic light scattering (DLS), and zeta potential measurements. The biocompatibility and cellular uptake were evaluated in MDA-MB-231 breast cancer cells, and MFH performance was tested in vitro. Following intravenous administration, MRI and MPI functionalities were analyzed through phantom studies and in vivo murine models.

Results: Coated M55 NPs displayed high colloidal stability in water and effective functionalization. The specific absorption rate (SAR) of 24.4 ± 1.4 W/g confirmed their suitability for MFH applications. In vitro assays indicated excellent biocompatibility and substantial cellular internalization, with GM55 showing the highest uptake and MFH efficiency, reducing cell viability to 50.62 ± 3.92% post two treatment cycles, compared to 67.71 ± 6.11% (CM55) and 71.39 ± 5.84% (PM55). MRI transverse relaxivity (r_2) values were notably high across all coatings, enhancing imaging contrast. MPI analysis demonstrated superior cell labeling sensitivity, with GM55 achieving the most pronounced detection. In vivo imaging confirmed effective NPs accumulation in the liver, underscoring their utility as dual MRI/MPI contrast agents (CAs).

Conclusion: Coated M55 NPs exhibit significant promise as multifunctional theranostic agents for cancer treatment. GM55, in particular, offers superior MFH efficacy and cellular uptake, while CM55 and PM55 may present unique advantages for alternative biomedical applications. The dual-imaging capabilities of these NPs provide a robust platform for real-time monitoring of distribution and therapeutic outcomes. Future investigations will focus on optimizing NPs formulations and expanding in vivo assessments to advance clinical translation.

Keywords: nanotheranostics, magnetic fluid hyperthermia, magnetic resonance imaging, magnetic particle imaging

Introduction

Despite the availability of various imaging techniques for cancer detection, their inherent limitations highlight the need for new technologies. In terms of treatment, traditional cancer therapies include chemotherapeutic agents, surgical procedures, thermal ablation, focused ultrasound, and radiation therapy. These treatments, however, often suffer from

Received: 21 November 2024
Accepted: 18 February 2025
Published: 29 March 2025

drawbacks such as systemic toxicity, limited targeting specificity, and the emergence of multidrug resistance.[1,2] To overcome these limitations, innovative approaches that can provide targeted, effective cancer treatment while minimizing side effects are being actively explored.

Recent advancements in nanotechnology have paved the way for innovative strategies to support cancer therapies, particularly using superparamagnetic iron oxide nanoparticles (SPIONs). Firstly, Magnetic Fluid Hyperthermia (MFH) utilizes SPIONs to apply localized heat to tumor lesions. When exposed to an alternating magnetic field (AMF), these NPs act as efficient mediators for heat exchange, facilitating targeted thermal energy delivery. Cancerous cells undergo apoptotic death at temperatures exceeding 42–43°C while neighboring healthy cells remain viable.[3,4] The thermal dose—defined as the duration of exposure at an elevated temperature (typically over 15 minutes at 42–43°C)[5] —can make hyperthermia directly cytotoxic,[6] sensitize cells to radiation[7,8] and chemotherapy,[9] enhance blood perfusion to reduce tumor hypoxia,[10] and stimulate anti-tumor immune signaling.[11]

Secondly, cell-based treatments, such as the administration of immune and stem cells, have emerged as promising approaches in cancer therapy. In this context, SPIONs are widely used as tracers for cell tracking. By incubating cells with SPIONs, researchers can monitor the migration and fate of these cells during therapy, providing valuable insights into treatment efficacy.[12,13]

For both novel applications, developing NP systems with specifically optimized properties is essential. Sensitive measurement of the location and exact quantity of injected NPs is crucial to determine their migration to target sites, assess their persistence, and ensure that sufficient doses—or cell numbers—are locally available.

The primary imaging modality traditionally used for this purpose is Magnetic Resonance Imaging (MRI) which shows favorable properties such as non-invasiveness, good sensitivity to magnetic NPs and the lack of ionizing radiation.[14,15] SPIONs have been widely studied and used as T_2 contrast agents (CA). However, a significant limitation of MRI for NPs monitoring is its inability to quantify the amount of iron locally present in tissues directly.

A relatively new and advanced imaging technique that can precisely locate and quantify magnetic NPs is Magnetic Particle Imaging (MPI). Unlike MRI, which detects iron oxide NPs indirectly, by their effect on water protons, MPI directly detects SPIONs as a positive signal, offering a spatial resolution of approximately 1 mm without interference from surrounding tissues. The MPI technique has been meticulously described and is gaining acceptance as a preclinical imaging modality.[16–18]

Materials with self-regulating temperature (SRT) properties—heating only up to their Curie temperature, the point at which a magnetic phase transition from ferromagnetic to paramagnetic occurs—offer a critical safety advantage in MFH by preventing overheating and minimizing damage to adjacent healthy tissues.

This study investigates the innovative NPs, named M55, developed by MBN Nanomaterialia S.p.a. (Treviso, Italy),[19] which leverages this intrinsic self-regulating feature. We focus on its potential as a theranostic, multimodal, and cell-labeling CA. Our previous research[6,20] demonstrated the efficacy of glucose-coated M55 (GM55) in slowing tumor growth after a single intratumoral injection and subsequent AMF treatment. In this work, we characterize both the hyperthermia performance and MPI properties of the M55 nanoparticle. This is particularly significant as MFH can be effectively conducted using MPI, which allows for precise localization and monitoring of the heating process.[3] By integrating MPI with MFH, millimeter-precision localized heating could be achieved, ensuring that therapeutic temperatures are applied selectively to tumor tissues while minimizing damage to surrounding healthy cells.[3]

Building on these promising findings, the goal of the present investigation was to explore whether alternative biological coatings—glucose, chitosan, and poly-ethylene glycol (PEG)—can further enhance M55's magnetic properties, imaging performance, therapeutic efficacy, and cell labeling capabilities. We characterize these coated NPs as bimodal CAs for MRI and MPI, evaluate their efficacy in MFH, and benchmark their performance against the commercial reference Ferucarbotran (marketed as VivoTrax® by Magnetic Insight Inc., Alameda, CA, USA), which is essentially a rebranded version of the Resovist® MRI CA. This in-depth analysis aims to advance our understanding of how specific surface coatings can enhance the multifunctional capabilities of M55 for diverse biomedical applications.

Materials and Methods

Nanoparticle Synthesis and Functionalization

The synthesis of doped ferrite NPs was conducted by MBN Nanomaterialia S.p.A. (Treviso, Italy) using a proprietary mechanochemical process,[19] as previously described.[6,20] Briefly, MgO, Fe_2O_3, and TiO_2 powders in a 4:2:1 molar ratio, respectively, were thoroughly mixed, and the reaction was carried out using ball milling equipment for 6 hours, in accordance with the procedure detailed in the cited patent.[21] A heat treatment at 1200 °C for 4 hours in air followed. The resulting powders were finely ball-milled for 1 hour, then homogeneously dispersed in isopropanol and ultrasonicated to promote de-aggregation. Centrifugation at 1000 g was used to extract nanosized particles (<200 nm). Detailed processing parameters are provided courtesy of MBN Nanomaterialia S.p.A.

NPs were coated with three organic materials: glucose, chitosan, and PEG. The glucose coating was carried out as previously described.[6] Briefly, iron-based NPs were first coated with citrate moieties using trisodium citrate dihydrate (≥99%, Sigma-Aldrich, St. Louis, MO, USA) as the reagent, followed by glucose capping using D-(+)-glucose (99%, Alfa Aesar, Haverhill, MA, USA). A microwave-assisted synthesis expedited the coating process. Specifically, 1 mL of M55 NPs suspension and 3 mL of 1 M sodium citrate solution were subjected to microwave heating at 90 °C for 7 minutes. After centrifugation, the process was repeated for glucose capping using a 1 M glucose solution. The resulting NPs were termed glucose-coated M55, or GM55.

The procedure involved two steps for the chitosan coating: the synthesis of O-carboxymethyl chitosan followed by the coating of NPs. O-carboxymethyl chitosan was synthesized as described by Chen and Park.[22] In brief, 1 g of chitosan (MW 15 kDa, DA 85%, Polysciences, Inc., Warrington, PA, USA) was suspended in 10 mL of a 2-propanol/H_2O (8:2) mixture with 1.35 g of NaOH (Thermo Scientific, Waltham, MA, USA) and left to swell for 1 hour at 40 °C. Next, 1.5 g of monochloroacetic acid (99%, Alfa Aesar, Haverhill, MA, USA) dissolved in 2-propanol was added dropwise to the chitosan suspension under vigorous stirring. The mixture was stirred at 40 °C for 4 hours, and the reaction was terminated by adding 20 mL of 70% ethanol. The product was centrifuged at 7000 g for 5 minutes and washed thrice with 70–90% ethanol. The final product was then dried under vacuum. For the NPs coating process, 8 mL of a 10 mg/mL solution of O-carboxymethyl chitosan (O-CMCH) was placed in a 50 mL round-bottom flask and stirred in an oil bath at 50 °C. Under vigorous stirring, 1 mL of M55 suspension (8 mg/mL) in 2-propanol was added dropwise to the O-CMCH solution and stirred at 50 °C for 24 hours. The suspension was centrifuged at 11000 g for 30 minutes at 40 °C, and the resulting NPs (CM55) were resuspended in deionized water and autoclaved at 121 °C for 20 minutes.

Similarly, PEG coating was carried out in two steps: synthesis of monomethyl PEG phosphate and NPs coating. Monomethyl PEG phosphate was synthesized following Boyer et al.[23] In brief, 4.00 g of monomethyl PEG (MW 2000, Sigma-Aldrich, St. Louis, MO, USA) were dried at 70 °C under vacuum overnight and cooled under an argon atmosphere. Twelve milliliters of anhydrous tetrahydrofuran (THF) were used to dissolve the PEG. Meanwhile, 374 µL of $POCl_3$ (99%, Sigma-Aldrich, St. Louis, MO, USA) dissolved in 2 mL of anhydrous THF were added dropwise to the PEG solution. The reaction mixture was stirred at 55 °C under argon for 6 hours, then cooled to room temperature. The solvent was removed using a rotary evaporator at 70 °C and dried under vacuum. The product was purified via dialysis in water, and the solvent was again removed using a rotary evaporator. Once monomethyl PEG phosphate was synthesized, it was used for PEG coating: 0.08 g of m-PEG-PO_4 were dissolved in 4 mL of water and transferred to a G30 glass vial with 1 mL of M55 suspension in 2-propanol (8 mg/mL). The mixture was heat-treated using a microwave oven reactor (Monowave 400, Anton Paar, Graz, Austria) at 90 °C for 10 minutes. The suspension was centrifuged at 9000 g for 10 minutes at 40 °C, and the resulting NPs (PM55) were resuspended in sterile deionized water.

Physicochemical Characterization

FT-IR spectra of coated NPs were measured with a Nicolet iS50 FT-IR spectrometer (Thermo Fisher, Waltham, MA, USA). Samples were prepared by dispersing 3 mg of powders of NPs in 300 mg KBr and preparing a pellet of 1 cm diameter.

The morphology of the NPs was observed on a Philips Morgagni 268 D electron microscope (Fei Company, Eindhoven, The Netherlands), equipped with a Megaview II camera (Evident Corporation, Tokyo, Japan) to acquire digital images. The sample was deposited on a copper grid and desiccated before the measurements.

For scanning electron microscopy (SEM) analysis, samples were deposited on metallic specimen stubs, and sputter-coated with gold (MED 010 Balzers). SEM imaging was performed by an XL30 ESEM (Fei Company, Eindhoven, The Netherlands).

The hydrodynamic size and zeta potential of the coated NPs were determined using a Malvern Zetasizer Nano instrument (Malvern Panalytical, Great Malvern, England). The sample was prepared in a suitable plastic cuvette, and its stability was monitored for a month. Zeta potential was measured on day 1, while Dynamic Light Scattering (DLS) measurements were carried out on days 1, 2, 3, 7, 14, and 28 to evaluate changes in particle size over time. The iron concentrations were quantified using inductively coupled plasma optical emission spectroscopy (ICP-OES) using an iCA RQ ICP-MS (Thermo Scientific, Waltham, MA, USA).

Magnetic Properties and Hyperthermia Evaluation

The ability to convert magnetic energy into heat of magnetic NPs, in the presence of an external AMF, is quantified from the specific absorption rate (SAR) value. The SAR value of NPs in solution is calculated by using the following equation:

$$SAR = C\frac{dT}{dt}\frac{m_s}{m_m}$$

where C is the specific heat capacity of the solvent (water = 4.186 J g^{-1} K^{-1}), dT/dt is the initial slope of the time-dependent heating curve, m_s is the mass of the solvent, and m_m is the mass of the magnetic NPs.

SARs were measured using a Nanotherics MagneTherm system (Warrington, UK), with samples diluted in water. Heat dissipation depends on both the frequency and amplitude of the applied AMF. Temperature variation within the samples was monitored at 1.0 s intervals using a multichannel thermometer equipped with optical fiber probes (FOTEMP4, Optocon AG, Dresden, Germany). The thermometer remained within the sample throughout the entire measurement period. The concentration of magnetic nanoparticles (MNPs) was 2 mg of Fe/mL. The AMF parameters were chosen in accordance with the Hergt criterion for clinical translatability,[24] specifically a magnetic field intensity of 15.9 kA/m and a frequency of 524.7 kHz. During the measurements, the samples were maintained at a constant temperature of 37 °C in a custom-built, closed chamber with a thermostatic air stream.

MRI and MPI Performance

Phantoms were prepared for in vitro MRI by suspending iron NPs (M55) in a range of concentrations: 200 μM, 100 μM, 50 μM, 25 μM, and 0 μM in distilled water (dH_2O), and the same was done for the commercially available CA Ferucarbotran (VivoTrax®, Magnetic Insight Inc., Alameda, CA, USA) as reference. MR imaging for quantification of the R_1 and R_2 relaxation rates was performed at ambient temperature (22 °C) on a 9.4T Bruker (Karlsruhe, Germany) BioSpec Avance III 94/20 system and a 7T Bruker (Karlsruhe, Germany) PharmaScan scanner, both equipped with a 72 mm internal diameter coil. All samples were positioned in an in-house 3D-printed rack for imaging.

The longitudinal relaxation times T_1 were measured, using a saturation recovery approach, with a fast spin-echo MRI pulse sequence (RARE, Rapid Acquisition with Relaxation Enhancement). In the saturation recovery approach, images are acquired using a range of repetition times (TR) and a fixed echo time (TE), determined according to the range of T_1 values to be measured. In this experiment, images were acquired with the following parameters: TR = 100, 337, 598, 890, 1220, 1600, 2050, 2600, 3300, 4285, 2925, and 12500 ms, TE = 8 ms, matrix size = 128 x 128, FOV = 40×40 mm^2, image in-plane resolution = 0.3512×0.3512 mm^2, slice number = 1, slice thickness = 1 mm, NEX = 1, RARE Factor = 2. T_1 relaxation maps were calculated using pixel-wise fittings of a saturation recovery model to the saturation time image series.

The transversal relaxation times T_2 were measured using a 2D Multi Spin Echo (MSE) pulse sequence. In this approach, a series of images are acquired using multiple echoes, with a range of TE values, and a fixed TR value. TE values are determined according to the range of T_2 values to be measured. This protocol acquired an image series with 64 spin-echo images in coronal orientation, covering a total echo time range from 8 ms to 512 ms, with the following major sequence parameters: TR = 10,000 ms, first TE = 8 ms, Echo spacing = 8 ms, 64 echoes, matrix size = 128 × 128, FOV = 40×40 mm^2, image in-plane resolution = 0.3125×0.3125 mm^2, slice number =1, slice thickness = 1 mm, NEX = 1. T_2 decay maps were calculated using pixel-wise fittings of a mono-exponential decay to the echo time image series.

From these maps, relaxation rates $R_1 = 1/T_1$ and $R_2 = 1/T_2$ were calculated in ROIs covering the individual sample tubes. NPs relaxivity was then estimated through linear fitting of R_1 and R_2 vs sample concentration [mM].

The MPI performance of NPs was evaluated using a pre-clinical MOMENTUM MPI scanner from Magnetic Insight, Inc. (Alameda, CA, USA). This involved acquiring two-dimensional projection images of sample vials and measuring the MPI relaxation properties of the particles in bulk samples. Based on these relaxation assessments, the particle-specific Point Spread Functions (PSFs) were determined for all specimens to evaluate the achievable resolution and signal for each particle type.

MPI relaxometry was conducted for all M55 coating variants (GM55, CM55, and PM55), in µPCR tubes containing 200 µL of particle suspension in H_2O equivalent to 100 µg of total Fe. An equivalent dose of Ferucarbotran was used as a reference to compare with a widely used standard MPI tracer. The amplitude of the PSF was normalized to the amount of iron to enable direct comparison of signal intensity. Expected imaging resolution (in mm) was determined from the particle PSFs by measuring the Full-Width Half-Maximum (FWHM), measured in units of the instantaneous strength of the scanner's drive field (in mT), and dividing by the field gradient used for the relaxation measurements (G = 5.7 T/m).

For MPI signal calibration, images were acquired in 2D with a 5.7 T/m selection field gradient and excitation field strengths of 20 and 26 mT in the X and Z channels, respectively to acquire a 12×6 cm FOV.

2D MPI of the empty sample holder was conducted at the beginning and end of the imaging sessions. The standard deviation of the background noise (SDnoise) was measured in these images. A threshold set at five times the SD noise was applied to quantify the signal to mask lower amplitude signals and ensure a reliable measurement of the MPI signal. Following the Rose Criterion, this imaging criterion is based on the MPI signal with a signal-to-noise ratio (SNR) greater than 5.[25] To determine the dependence of signal strength on particle concentration (and assess signal linearity and particle detection limits) 11 samples for each NPs (GM55, CM55, PM55 and Ferucarbotran) were imaged with identical parameters in a decreasing series in dH_2O containing 200, 100, 50, 25, 12.5, 10, 8, 6, 4, 2, and 1 µg of Fe. The total MPI signal was calculated as the MPI signal integral within a region of interest (ROI) of pixels with a signal higher than 5*SDnoise.

Cytotoxicity and Labeling Studies

MDA-MB-231 human breast cancer cells and WI-26 human lung fibroblasts were purchased from ATCC (Manassas, VA, USA) and cultured in Dulbecco's modified Eagle's medium (DMEM) (Gibco, Thermo Fisher Scientific, MA, USA) + 10% fetal bovine serum (FBS) + 1% P/S + 1% L-Glut.

To assess the cytotoxicity of GM55, CM55 and PM55, for both cell lines, 5000 cells were seeded in each well of a 96-well plate and incubated for 24 hours at 37 °C in humidified air with 5% CO2. The medium was then replaced with fresh medium, containing 75, 50, 25, 12.5, 6.25 and 0 µgFe/mL of NPs. Cytotoxicity was assessed through the MTT (3-(4,5-dimethylthiazol-2-yl)-2,5-diphenyltetrazolium bromide) assay after 24 and 48 hours of incubation. Then, 100 µL of MTT solution (5 mg/mL) were added to each well and incubated for 4 h. Then, the MTT solution was removed and 100 µL of dimethyl sulfoxide (DMSO) was added to each well to dissolve the formazan crystal. Absorbance was read using an HTX microplate reader (BioTek Instruments, Winooski, VT, USA) at a wavelength of 570 nm. Four measurements of optical density (OD) were recorded for each sample, and cell viability (%) was calculated with the following equation: CV% = (ODsample/ODcontrol) × 100.

Once the maximum non-toxic concentration was determined, MDA-MB-231 cells were labeled using a previously reported protocol with some modifications.[20] Briefly, 3×10^5 MDA-MB-231 cells were seeded for labeling on coverslips in 6-well plates. After 24 h, 50 µgFe/mL of NPs were added to complete media and left to co-incubate for 24 hours and 48 h. The cells were washed twice with Phosphate-Buffered Saline (PBS) 1X, fixed with 4% paraformaldehyde for 20 min, and then washed. Next, the NPs in cells were stained with Hematoxylin and Eosin and Prussian Blue. For Prussian Blue staining, cells were incubated with a freshly prepared mixture of 2% potassium ferrocyanide and 2% HCl (1:1 volume mix) for 30 min at room temperature. After washing three times, the cells were counterstained with nuclear fast red for 5 min. Then, the coverslips were removed from the 6-well plate, dehydrated in ethanol, cleared in xylene and mounted in Entellan mounting medium (Merck, Kenilworth, NJ, USA). The stained cell samples were observed using an Olympus APX100 (Evident Corporation, Tokyo, Japan).

Transmission Electron Microscopy (TEM) analysis was conducted to confirm the uptake and internalization of NPs by the MDA-MB-231 cell lines. After 2-, 6-, and 24 hours of incubation, the cells-NPs were fixed in 2.5% (w/v)

glutaraldehyde in 0.2 M sodium phosphate buffer at 4 °C overnight, post-fixed in 1% osmium tetroxide in 0.2 M sodium buffer, dehydrated in a graded series of ethanol, infiltrated with a mixture of Epon and Araldite resins and polymerized using an oven at 60 °C for 24 h. Ultrathin sections (70 nm) were cut using a diamond knife (Diatome) and collected onto TEM grids. Two grids were collected from duplicate regions for each sample and imaged using a Philips Morgagni 268 D electron microscope (Fei Company, Eindhoven, NL, USA) equipped with a Mega View II camera (Olympus, Tokyo, Japan) for the acquisition of digital images.

In vitro Hyperthermia

To evaluate the efficacy of NPs in MFH, 10,000 MDA-MB-231 cells were seeded into 8-chamber slides. Following a 24-hour incubation, NPs were added at a 50 μgFe/mL concentration. After another 24-hour incubation period, free NPs were removed by washing the cells thrice with 4°C PBS (1X). The cells were then placed in a custom-built sealed chamber with a thermostatically controlled air stream maintained at 37 °C. Cells were exposed to an AMF with a nominal frequency of 523.4 kHz and a maximum field strength of 20 mT (equivalent to 15.9 kA/m) for 20 minutes. Both single and consecutive treatments (24 hours apart) were applied. The effectiveness of the MFH treatment was measured using the MTT assay as described in the previous paragraph. Control groups included untreated cells, and cells incubated with 50 μgFe/mL NPs without exposure to MFH. Twenty-four hours after the final MFH treatment, cytotoxicity assays were conducted to assess cell viability, which was then normalized to the corresponding control groups. The viability of MDA-MB-231 cells was compared after one or two hyperthermia treatments.

Cellular Imaging

For MRI and MPI imaging, cells were seeded and treated as described in "Cytotoxicity and Labelling Studies". After the incubation time, cells were washed 3 times with 4 °C PBS, trypsinized and centrifuged at 125 g x 5 minutes. Cell pellets were washed 3 more times to get rid of all the non-internalized NPs. Samples were prepared, in duplicate, in a dilution series: 200, 100, 50, 25, 12.5, 6, 3, 1.5, 0.75 ($\times 10^3$) cells, and then imaged. MPI imaging was conducted using the same parameters as for phantoms. The 1.5 mL Eppendorf tubes containing the cell pellet were scanned using a custom 3D printed imaging bed, allowing the imaging to occur in an identical location.

We defined MPI in vitro cell detection limits as the minimum number of MDA-MB-231 cells detected with SNR > 5*SD of the signal of the control cells (without exposure to NPs). Thus, cells with a signal below the $5*SD_{\text{unlabelled cells}}$ criteria were considered undetected. The amount of Fe internalized by the cells was calculated as iron signal/number of cells.

Cell pellets were also prepared in the bottom of 0.2 mL Eppendorf tubes, for MRI imaging. A gradient echo (FLASH) acquisition sequence was used, with the following parameters: TR = 500 ms, TE = 6 ms, flip angle = 30°, FOV = 30×58 mm^2, matrix size = 384 × 384, NEX = 1, slice thickness = 1mm. In this study, the acquisition parameters were optimized to maximize the detection of signal voids induced by NPs while maintaining homogeneous signal intensity from surrounding water.

In vivo Studies

All procedures were conducted following the Australian Code of Practice for the Care and Use of Animals for Scientific Purposes and were approved by the University of New South Wales Animal Care and Ethics Committee (ACEC Number: 23/104B). During the scanning procedure, general anesthesia was induced in an induction chamber with 4% isoflurane in oxygen (0.8 L/min) and maintained at 1–2% isoflurane at 0.8 L/min oxygen flow rate through a nose cone. Respiratory rate was monitored during the imaging procedures using a pressure-sensitive pad. Animal body temperature was kept stable using a circulating water-warming blanket.

In vivo imaging was performed on a Bruker (Karlsruhe, Germany) 9.4 T BioSpec Avance III 94/20 magnetic resonance microimaging system equipped with a 35 mm internal diameter birdcage volume coil.

Animals (8–12 weeks old, n = 3 per group; BALB/cJAusb, Ozgene ARC, Perth; WA, Australia) were scanned with MRI and MPI before injection. After 30 minutes from either GM55, CM55, PM55 or Ferucarbotran injection through the tail vein (dose = 4 mgFe/kg), animals were culled to freeze NPs biodistribution and then imaged again with both MRI and MPI.

MRI T_2-weighted images were acquired using a 2D Fast Spin Echo Sequence (RARE) with the following parameters: TR = 1800 ms, TE = 21 ms, NEX = 6, field of view = 40×80 mm^2, MTX = 200 × 400, slice thickness = 1 mm, FA = 90°, Echo Train Length = 4. The parameters of this sequence were selected to ensure an optimal SNR and enhance sensitivity to the presence of NPs at the same time.

MPI images were acquired in 2D with a 5.7 T/m selection field gradient and excitation field strengths of 20 and 26 mT in the X and Z channels, respectively.

Statistical Analysis

All statistical analyses were conducted using GraphPad Prism v.10 (GraphPad Software, Boston, MA, USA). Linear regression was used to fit R_1 and R_2 values against iron concentrations to determine NPs' longitudinal (r_1) and transverse (r_2) relaxivity. A two-way ANOVA was performed to compare cell viability results across different NPs coatings and hyperthermia treatment conditions, followed by Dunnett's post-hoc test. P values of $p < 0.05$ were considered statistically significant.

Results

Physicochemical Characterization

The uncoated M55 and its glucose-citrate coated variant GM55 were previously characterized by Vurro et al.[20] Briefly, by comparison of the X-Ray Powder Diffraction (XRPD) patterns with database ones (PDF-4), it was found that M55 consists of a mixture of hematite (α-Fe_2O_3), magnesium ferrite ($MgFe_2O_4$), and magnesium titanate ($MgTiO_3$) in a mass ratio of 10:60:30. The XRPD spectra obtained in this study were perfectly superimposable with those previously reported by our group,[6,20] further confirming the consistency and reproducibility of the crystalline composition. Moreover, FT-IR spectra confirmed the presence of both citrate ions and glucose molecules as capping agents on the NPs surface.

As shown in Figure 1a, the analysis of the FTIR spectrum for CM55 NPs reveals the presence of o-carboxymethyl chitosan (OCMCH) on the NPs surface. In fact, a broad absorption at ~3500 cm^{-1} is attributed to -OH group stretching vibration, while the one at 2900 cm^{-1} is due to vibrations of C-H bonds. A strong peak at 1600 cm^{-1} is attributed to overlapping stretching vibrations of carbonyl groups from N-acetylamide residues and of carboxylate groups of the carboxymethyl moieties. Additionally, the broad band in the 900–1200 cm^{-1} range confirmed the presence of C-O and C-OH bonds in the chitosan structure. The region between 800 and 2000 cm^{-1} has been zoomed in Supplementary Materials (Figure S1), to better visualize such broad band.

Figure 1b shows the FTIR spectrum of the PM55 sample, demonstrating the presence of phosphate-PEG on the NPs surface, as evidenced by absorption bands at 2900 cm^{-1} and 1460 cm^{-1}, corresponding to C-H stretching and bending vibrations of PEG. The four characteristic features in the 1400–1200 cm^{-1} region are slightly shifted in the PM55

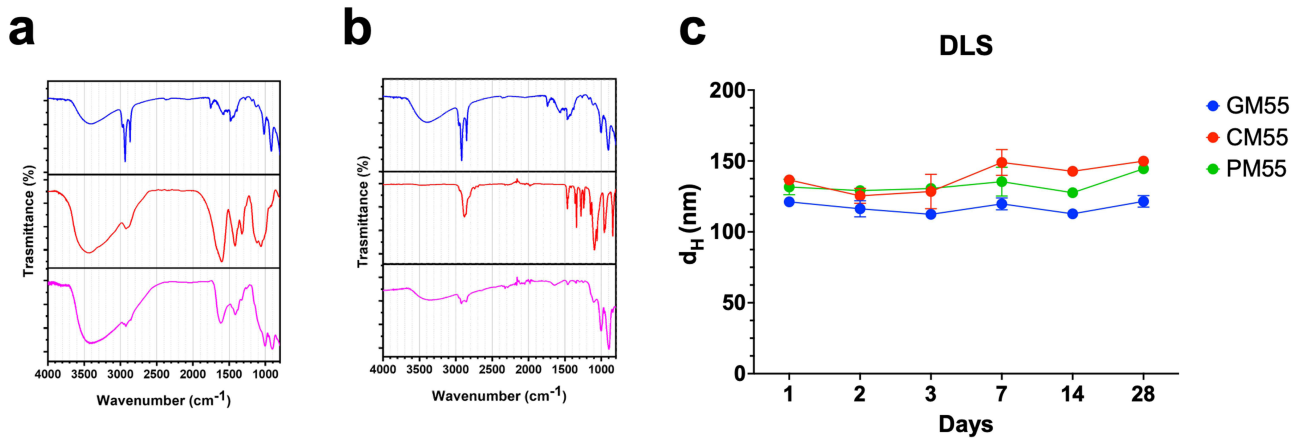

Figure 1 Physicochemical characterization of M55 and coated-M55 NPs. (**a**) FTIR spectra of bare M55 NPs (blue line), o-carboxymethyl chitosan (red line) and CM55 (pink line). (**b**) FTIR spectra of bare M55 NPs (blue line), phosphate PEG (red line) and PM55 (pink line). (**c**) Hydrodynamic diameter (d_H) of GM55, CM55, and PM55 measured by DLS over a period of 28 days. The stability of the hydrodynamic diameter across all three coatings indicates good colloidal stability of the NPs in solution.

https://doi.org/10.2147/IJN.S506443

spectrum with respect to the phosphate-PEG one, indicating that the phosphate-PEG is bound to the NPs surface. A strong absorption band around 1100 cm^{-1} observed in the PM55 spectrum, is characteristic of C-O bonds of the phosphate-PEG molecule.

Figure 1c illustrates the hydrodynamic diameters of GM55, CM55, and PM55 NPs over a 28-day period, highlighting good stability, with consistent hydrodynamic sizes observed throughout the duration.

The zeta potential values, expressed as mean ± standard deviation from three replicates, were −34.0 ± 1.3 mV for GM55, −19.3 ± 0.6 mV for CM55 and −20.7 ± 0.5 mV for PM55, indicating very good colloidal stability of these NPs in aqueous dispersions. To provide a clearer visualization of the zeta potential dispersion, as well as to confirm particle size consistency with DLS measurements, the Supplementary Material provides relevant zeta potential plots (Figure S2) along with TEM (Figure S3) and SEM images (Figure S4).

Magnetic Properties and Hyperthermia Evaluation

Thermal profiles were recorded from a baseline bulk temperature of approximately 37.0 °C, selected to replicate in vivo conditions. The SAR for all M55 NPs formulations in aqueous solution, measured at a consistent iron concentration, was 24.4 ± 1.4 W/g, while Ferucarbotran exhibited a higher SAR of 59.3 ± 1.6 W/g. The thermograms of coated M55 NPs and Ferucarbotran are provided in Supplementary Materials (Figure S5).

MRI and MPI Performance

T_1 and T_2 relaxation times of water dispersions containing GM55, CM55, PM55, and Ferucarbotran were measured at 7T and 9.4T. Linear models were fitted to R_1 and R_2 versus Fe concentration to determine the longitudinal (r_1) and transverse (r_2) relaxivities. Figure 2a depicts the transverse relaxation rates alongside the linear regression lines at both field strengths. Since the corresponding longitudinal relaxations did not exhibit any dependence on concentration, these datasets are not presented here. All relaxivities, summarized in Figure 2b, underscore the significant transverse relaxivity (r_2) and negligible longitudinal relaxivity (r_1) of the NPs—characteristic behavior of Fe-based NPs.

The NPs' MPI performance was evaluated and compared against the commercial Ferucarbotran. The resulting PSFs are shown in Figure 2c. The following normalized peak signal intensities were determined from these: 4.003 a.u. (100%) for Ferucarbotran, 1.809 a.u. (36.0%) for GM55, 1.723 a.u. (29.5%) for CM55, and 1.512 a.u. (30.7%) for PM55. The corresponding PSF FWHM were measured to be 10.6 mT for GM55, 10.5 mT for CM55, 11.1 mT for PM55 and 13.2 mT for Ferucarbotran, which results in a calculated resolution at maximum field gradient of 5.7 T/m of our scanner of 1.89 mm, 1.84 mm, 1.94 mm, and 2.31 mm for GM55, CM55, PM55 and Ferucarbotran, respectively. Data are summarized in Figure 2d.

The integral signal intensities as measured from 2D MPI projection images of vials with different Fe concentrations are shown in Figure 2e. All NPs demonstrated a robust linear relationship between the signal quantified and the amount of iron ($R^2 > 0.99$). The total signal per µg of Fe was calculated and resulted in 11027 ± 45.58 a.u./µgFe for GM55, 8995 ± 66.11 a.u./µgFe for CM55, 9373 ± 52.28 a.u./µgFe for PM55, and 30731 ± 64.92 a.u./µgFe for Ferucarbotran.

Cytotoxicity and Labeling Studies

Before using NPs as hyperthermia mediators or cell tracking agents, evaluating their biocompatibility through in vitro cytotoxicity assays is essential. Figure 3a illustrates the cytotoxicity of GM55, CM55, and PM55 NPs after 24 and 48 hours of incubation with MDA-MB-231 cells at various concentrations of NPs. The MTT assay indicated that only the highest concentration of 75 µgFe/mL caused slight toxicity after 48 hours, regardless of the coating. No statistically significant differences in cell viability were observed at lower concentrations, leading to the selection of 50 µgFe/mL as the maximum non-toxic concentration.

Importantly, cytotoxicity assays conducted on the non-cancerous cell line, WI-26 fibroblasts, demonstrated that none of the tested concentrations is toxic. Toxicity data for fibroblasts are provided in the Supplementary Materials (Figure S6).

Following the determination of the maximum non-toxic concentration, NPs internalization by MDA-MB-231 cells was assessed. Hematoxylin and Eosin, alongside Prussian Blue staining (Figure 3b), confirmed successful NPs uptake at both 24 and 48 hours. The cells retained normal morphology throughout the incubation, suggesting minimal cytotoxicity

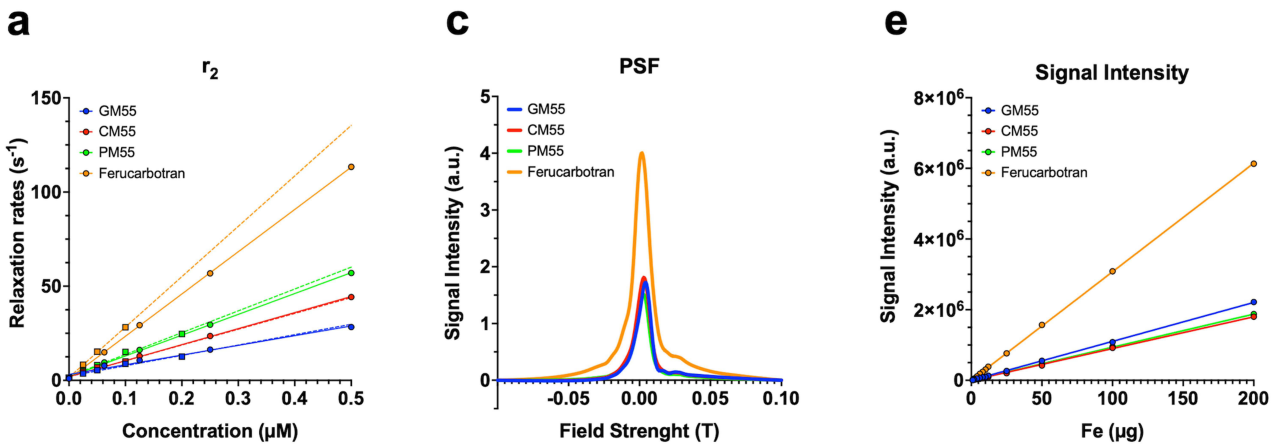

b

	r_1 ($mM^{-1}s^{-1}$)				r_2 ($mM^{-1}s^{-1}$)			
	GM55	CM55	PM55	Ferucarbotran	GM55	CM55	PM55	Ferucarbotran
7T	-0.01 ± 0.30	-0.01 ± 0.31	-0.02 ± 0.30	1.61 ± 0.30	51.50 ± 3.15	85.25 ± 1.95	110.60 ± 1.91	224.50 ± 1.00
9.4T	-0.19 ± 0.43	-0.12 ± 0.44	-0.14 ± 0.42	0.61 ± 0.46	55.09 ± 2.26	84.05 ± 1.98	115.90 ± 2.17	267.60 ± 1.59

d

	GM55	CM55	PM55	Ferucarbotran
FWHM (mT)	10.6	10.5	11.1	13.2
Resolution (mm)	1.89	1.84	1.94	2.31

Figure 2 Comparative evaluation of MRI and MPI performances of M55 variants (GM55, CM55, PM55) and Ferucarbotran (VivoTrax®). (**a**) Transversal relaxation rates (r_2) as a function of Fe concentration (R^2 > 0.98 in all samples) at 7T and 9.4T. Circles and continuous lines represent data acquired at 7T, while squares and dashed lines correspond to data acquired at 9.4T, illustrating the differences in relaxivity between the two field strengths. (**b**) Summary table of longitudinal (r_1) and transverse (r_2) relaxivities at 7T and 9.4T for each NPs, indicating negligible longitudinal relaxivity (r_1) and significant transverse relaxivity (r_2) for M55 variants. (**c**) PSFs of GM55, CM55, PM55, and Ferucarbotran NPs. (**d**) Comparison of FWHM and spatial resolution between NPs. (**e**) Integral signal intensity in 2D MPI projection images vs mass of iron across the tested NPs.

induced by the NPs. Prussian Blue staining specifically identified the presence of iron, further verifying internalization. Notably, PM55 NPs appeared to adhere more strongly to the coverslips than GM55 and CM55.

TEM provided additional insights into the internalization mechanisms. TEM images in Figure 3c demonstrated that NPs were internalized via endocytosis and subsequently encapsulated within endosomes that fused with phagosomes. These structures are involved in the degradation of cellular components, confirming that NPs undergo processing through the endosomal-phagosomal pathway. This internalization mechanism was consistent across all tested NPs coatings.

In vitro Hyperthermia

To investigate the application potential of different coatings in vitro experiments, M55 NPs with various coatings were tested as hyperthermia mediators on the triple-negative mammary carcinoma cell-line MDA-MB-231. As shown in Figure 4a, a single AMF application significantly reduced cell viability, independent of the coating, compared to control groups (untreated cells and cells incubated with NPs without MFH exposure). Interestingly, after two AMF treatments (Figure 4b), GM55 demonstrated superior efficacy in reducing the viability of MDA-MB-231 cells compared to CM55 ($p < 0.05$) and PM55 ($p < 0.05$). Specifically, cells treated with GM55 and exposed to AMF exhibited a viability of 79.12 ± 2.46% after the first treatment and 50.62 ± 3.92% after the second. In comparison, CM55-treated cells exposed to AMF showed viability rates of 81.18 ± 1.75% and 67.71 ± 6.11% after the first and second treatments, respectively. PM55-treated cells exposed to AMF had viability percentages of 83.39 ± 1.21% and 71.39 ± 5.84% following one and two treatments, respectively.

https://doi.org/10.2147/IJN.S506443

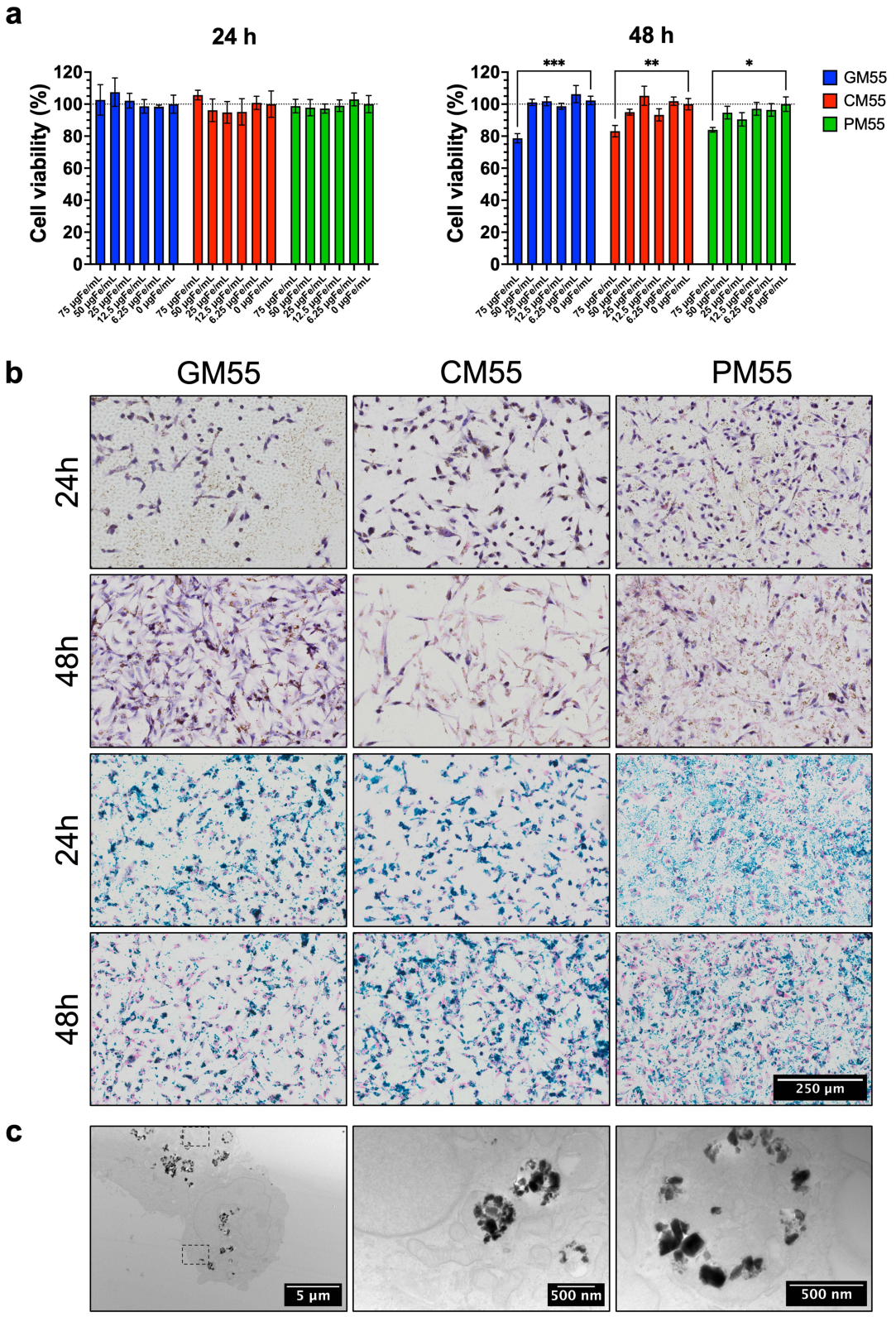

Figure 3 Cytotoxicity, cellular uptake, and NPs internalization of M55 variants in MDA-MB-231 cells. (**a**) Cell viability assessed using the MTT assay after 24 hours and 48 hours of incubation with GM55, CM55, and PM55 NPs at different concentrations. Data are presented as mean ± standard error of the mean (SEM). Statistical significance was evaluated using two-way ANOVA followed by Dunnett's post-hoc test (*$p < 0.05$, **$p < 0.01$, ***$p < 0.001$). (**b**) Hematoxylin and Eosin staining (top panels) and Prussian Blue staining (bottom panels) of MDA-MB-231 cells after incubation with GM55, CM55, and PM55 for 24 and 48 hours. Scale bar = 250 µm. (**c**) TEM images showing internalization of GM55 NPs in MDA-MB-231 cells after 24 hours of incubation. Scale bars: left = 5 µm, center and right = 500 nm.

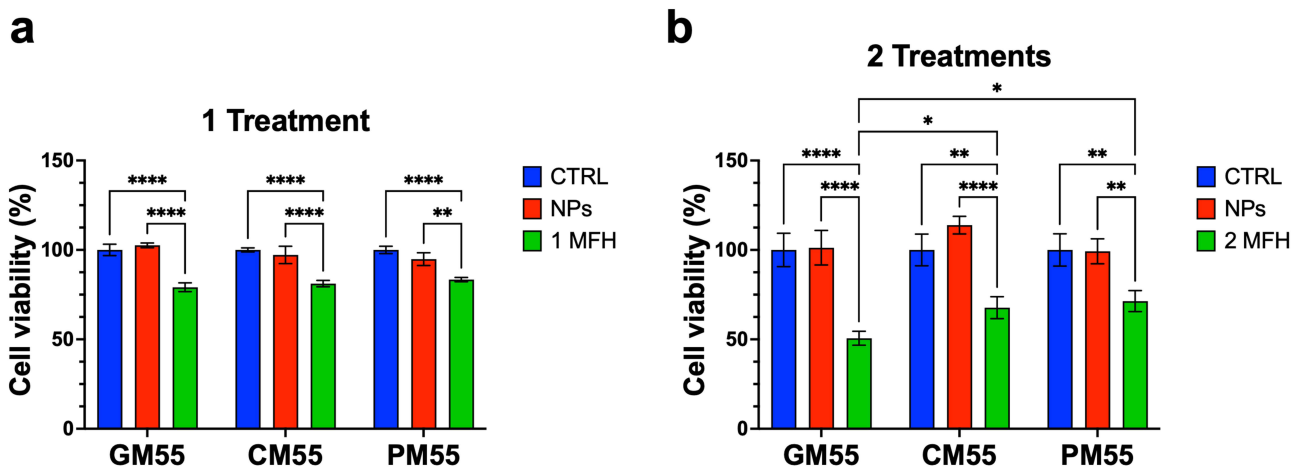

Figure 4 Magnetic fluid hyperthermia efficacy of M55-coated NPs. (**a**) Cell viability assessed by the MTT assay after exposure to either one or (**b**) two cycles of MFH treatment. Data are presented as mean ± standard error of the mean (SEM). Statistical significance was determined using two-way ANOVA followed by Dunnet's post-hoc test (*p < 0.05, **p < 0.01, ****p < 0.0001).

Cellular Imaging

Figure 5a presents representative MPI images of phantoms containing decreasing numbers of cells labeled with NPs. Using 2D MPI, the minimum detectable cell number was 6000 cells for GM55 after 24 hours of incubation, with a total signal more significant than 5 times the standard deviation (5*SD), corresponding to 152 ng of iron. For both CM55 and PM55, the minimum detectable count was 12,000 cells, corresponding to 141 ng and 173 ng of iron, respectively.

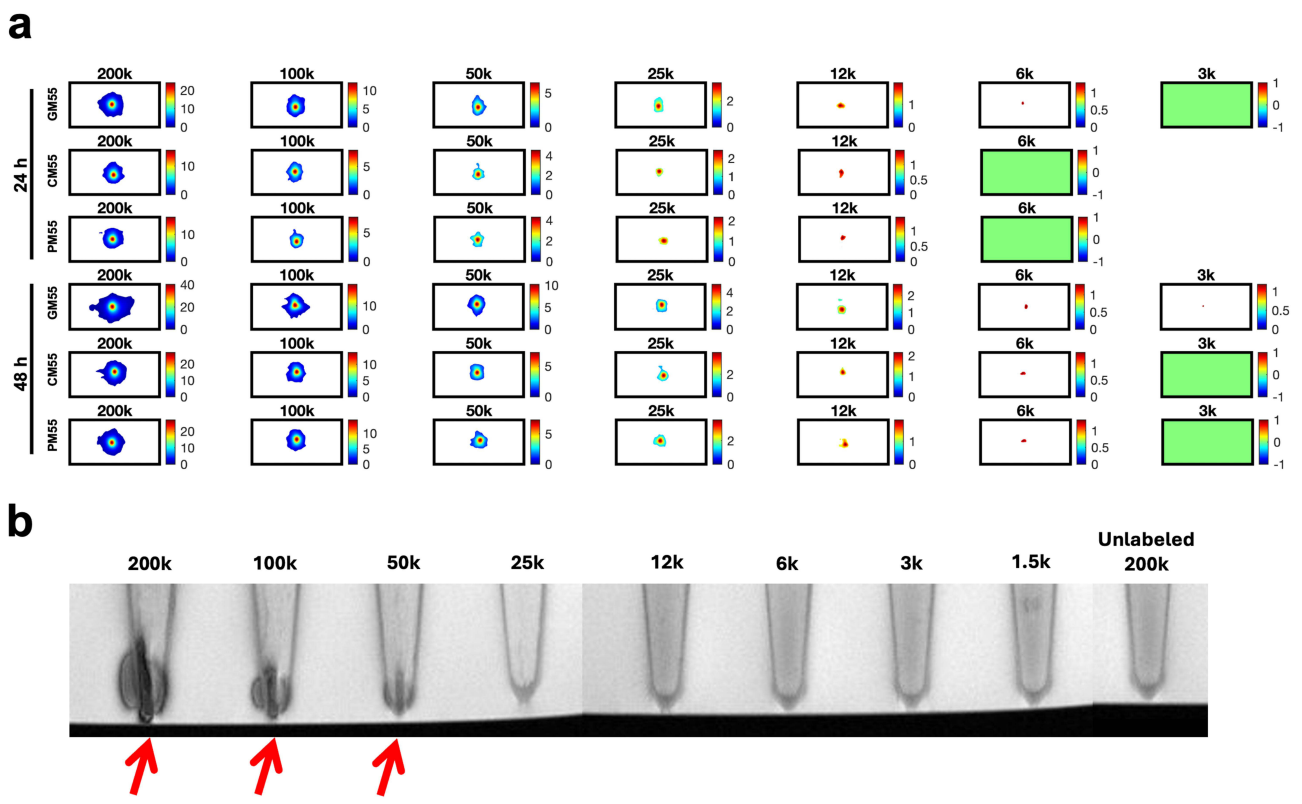

Figure 5 Cellular imaging of M55-labeled MDA-MB-231 cells. (**a**) MPI images of MDA-MB-231 cells labeled with GM55, CM55, and PM55 at different cell numbers (ranging from 200k to 3k cells) after 24 and 48 hours of incubation. Each frame displays MPI signal intensity above 5 times the standard deviation (5*SD), with higher intensities represented in red and green indicating a signal of 0. (**b**) Representative MRI images of cell pellets labeled with GM55, NPs at varying cell numbers. Signal voids attributable to NPs presence is clearly visible (indicated by red arrows) in samples with 50k cells or more, while no signal void is observed in the control (unlabeled) sample.

https://doi.org/10.2147/IJN.S506443

Notably, detection sensitivity improved after 48 hours of incubation: the minimum detectable cell number decreased to 3000 cells for GM55 (82 ng of iron) and 6000 cells for CM55 and PM55 (109 ng and 146 ng of iron, respectively).

The iron content per cell was estimated at approximately 25 pgFe/cell for GM55, 12 pgFe/cell for CM55, and 14 pgFe/cell for PM55 after 24 hours, increasing to 27 pgFe/cell for GM55, 18 pgFe/cell for CM55, and 24 pgFe/cell for PM55 after 48 hours. These values were corroborated by ICP-OES measurements, which showed similar iron content: 22.40 pgFe/cell for GM55, 13.35 pgFe/cell for CM55, and 14.90 pgFe/cell for PM55 after 24 hours, and 24.75 pgFe/cell for GM55, 19.15 pgFe/cell for CM55, and 22.98 pgFe/cell for PM55 after 48 hours.

Labeled cells were also detectable by MRI, with signal voids visible for up to 50,000 cells under all conditions. Control tubes containing unlabeled cells showed no such signal voids. Figure 5b shows a representative series of MRI images of cell pellets collected after 48 hours of incubation with GM55 in 0.5 mL Eppendorf tubes, where hypointense spots (indicated by arrows) correspond to the presence of M55 NPs within the cells. This result confirms our previous findings.[20]

In vivo Biodistribution

In vivo experiments were conducted to evaluate the potential of M55 NPs as bimodal CAs (CAs). Figure 6 displays representative MRI and MPI images from a mouse model. A significant reduction in signal intensity was observed, compared to the pre-contrast image (Figure 6a), in the liver 30 minutes post-contrast, as illustrated in Figure 6b. MPI provides a direct and absolute measurement of tracer location and quantity, as demonstrated in Figure 6c. The overlay of the MPI tracer concentration map of GM55 on the corresponding MRI image highlights the tracer's presence in the liver, confirming the detection of M55 NPs. Although MPI offers lower spatial resolution than MRI, it does not require relative measurements for visualization.

Quantitative analysis of the MRI SNR in the liver for all NPs variants is presented in Figure 6d, and the relative behavior was consistent across the different NPs coatings. However, it should be noted that the analysis from MRI images requires pre- and post-contrast images to appreciate the signal reduction.

These results effectively demonstrate the utility of M55 as a bimodal CA, highlighting the complementary information provided by MRI and MPI. The clear visibility of M55 NPs in both imaging modalities underscores their potential for multimodal imaging applications in medical diagnostics.

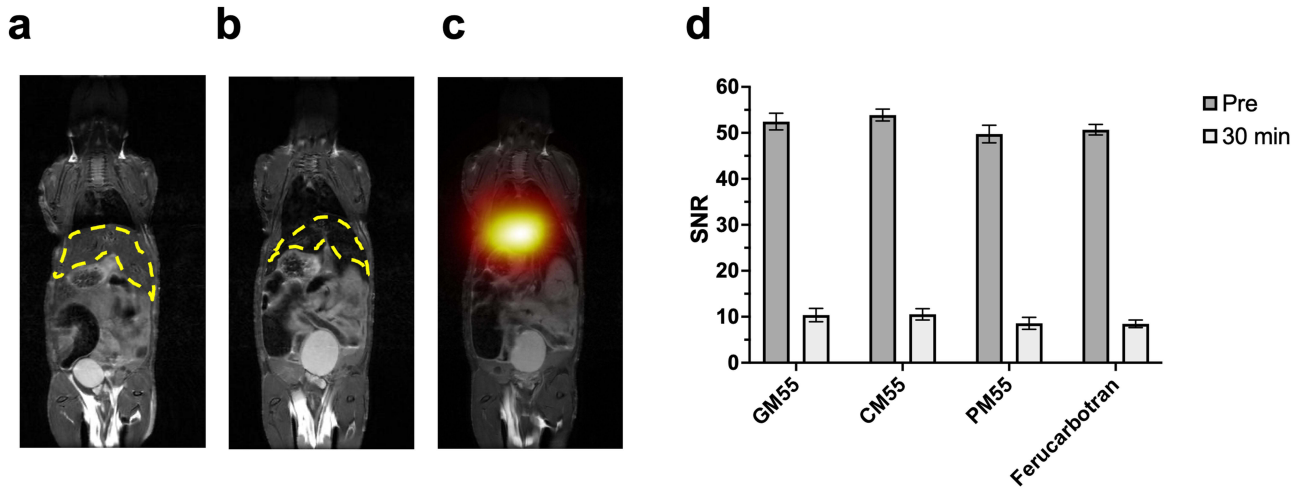

Figure 6 In vivo MRI and MPI biodistribution of G-M55 in a mouse model. (**a**) Pre-contrast MRI image. (**b**) MRI image 30 minutes after intravenous administration of GM55, showing significant negative contrast enhancement in the liver region (outlined in yellow). (**c**) Overlay of MRI and MPI images, demonstrating localization of GM55 signal in the liver. (**d**) MRI SNR of the liver for different CAs (GM55, CM55, PM55, and Ferucarbotran) at pre-contrast and 30 minutes post-contrast, illustrating consistent behavior across agents.

Discussion

The results of this study underscore the potential of M55 NPs, coated with glucose (GM55), chitosan (CM55), and PEG (PM55), as multifunctional agents for cancer theranostics. The mechanochemical synthesis of the metallic core ensures high reproducibility of key properties such as composition, SAR, and particle size. This reliability is evident when comparing the present results with our previous studies performed using different batches of the same NPs, where parameters like hydrodynamic size, SAR, and relaxivity remain consistent.[6,20,26]

We evaluated their physicochemical properties, MFH performance, dual-imaging capabilities (MRI and MPI), cytotoxicity and cellular uptake studies. These findings highlight the versatility of M55 as a promising platform for simultaneous imaging and therapy, effectively shortening the gap between diagnostic and treatment approaches for cancer.

Our results show that M55 NPs effectively enhance MRI contrast, thanks to their significant transverse relaxivity (r_2) values. While these values are lower than the significantly higher relaxivity of Ferucarbotran and slightly less than that of Ferumoxytol (Feraheme®) at 111.74 ± 3.76 $mm^{-1}s^{-1}$, measured at 3T,[27] and Ferumoxides (Endorem®) at 98.3 $mM^{-1}s^{-1}$,[28] our M55 NPs still demonstrate adequate MRI contrast capabilities.

MPI analysis demonstrated robust signals and high detectability of the coated M55 NPs. Unlike MRI, which requires relative measurements due to its inability to quantify iron content directly, MPI delivers a clear and positive signal from superparamagnetic iron oxide NPs without interference from background tissues. Although the signal intensity of coated M55 NPs was lower than that of Ferucarbotran and another maghemite core with nanoflower structure (trade name: Synomag-®D, Micromod Partikeltechnologie),[29] their spatial resolution was slightly better than Ferucarbotran's, making M55 NPs suitable for precise imaging applications. This combination establishes M55 NPs as effective dual-imaging CAs. By leveraging the direct visibility and linear relationship between tracer concentration and signal in MPI, M55 NPs facilitate accurate visualization and absolute quantification of NPs localization, thereby enhancing diagnostic precision.

Given the critical role of tracers in cellular therapies for monitoring cell biodistribution and dosage, we assessed cytotoxicity, cellular uptake and labeling efficiency of our NPs. Our results confirmed the excellent biocompatibility of these NPs with cancerous and non-cancerous cells, further supporting their suitability for biomedical applications. The efficient internalization of M55 NPs into MDA-MB-231 cells is supported by Prussian Blue staining, TEM analysis, MPI, and ICP-OES measurements. Both MRI and MPI could detect M55-labeled cells, though with different sensitivities. GM55 demonstrated the highest uptake efficiency at 24 and 48 hours of incubation, making it ideal for cellular studies. Interestingly, while PM55 showed similar internalization to GM55 after 48 hours of incubation, the MPI images of 3000 PM55-labeled cells did not yield signal intensities above 5 times the standard deviation of background noise, rendering this number of cells undetectable in MPI.

Each NPs coating imparts distinct advantages for specific applications. GM55, with its enhanced cellular uptake, is well-suited for cell tracking and intracellular MFH, potentially facilitated by glucose transporters on the cell membrane. CM55, featuring a chitosan coating, offers biocompatibility and mucoadhesive properties due to its cationic nature.[30] In contrast, PM55, coated with PEG, provides "stealth" characteristics, reducing recognition by the reticuloendothelial system (RES) and extending circulation time, making it advantageous for blood pool imaging and targeted intravascular applications.[31,32] However, a limitation of this study is that we did not directly assess these properties experimentally; instead, our conclusions are inferred from established findings in the literature. Future work should include a direct evaluation of these properties to confirm and further understand the coatings' specific effects in our system.

M55 NPs also exhibit strong MFH capabilities, generating localized heat that induces apoptosis in tumor cells while sparing healthy tissue.[3,4] The SAR of M55 surpasses Ferumoxytol's (10.4 W/g) but is lower than Ferucarbotran and Synomag-D (40.0 W/g).[33] This indicates that M55 NPs possess comparable heating efficiency to these commercial alternatives. Moreover, M55 feature an SRT near the Curie temperature, where they transition from ferromagnetic to paramagnetic, ceasing heat production and preventing overheating. This unique property ensures safe hyperthermia treatment, capable of inducing cell death or sensitizing tumors for adjunctive therapies like radiation or chemotherapy.[7,8] The SRT mechanism of M55 NPs, with a composition-dependent Curie temperature, allows for precise control of the maximum temperature reached, enabling selective damage to cancerous cells while preventing overheating of

surrounding healthy tissue. This intrinsic safety mechanism is particularly beneficial for hyperthermia applications, as it ensures that the therapeutic temperature does not exceed safe levels, thereby protecting healthy tissues.

Overall, M55 NPs represent a versatile solution for cancer theranostics, addressing critical limitations of conventional treatments. Their multifunctionality enables them to act as effective CAs for MRI and MPI while serving as cellular labels. The SRT property allows for repeatable, controlled hyperthermia, delivering therapeutic heat to tumors without harming adjacent healthy tissues. This targeted imaging and therapy combination offers a promising approach for more effective and safer cancer treatments.

The balance between heating performance and biocompatibility makes M55 NPs well-suited for applications requiring effective and safe hyperthermia treatment, offering a compelling advantage in cancer therapy.

For the first time, the in vivo biodistribution studies demonstrated that M55 NPs can serve as CAs for MPI, complementing their MRI capabilities. Their observed accumulation in the liver is consistent with clearance via the RES, which, while challenging for systemic applications, provides potential for liver-targeted imaging and therapy.

While M55 NPs demonstrate promising multifunctional properties, their performance in certain aspects, remains lower than that of some commercially available nanoparticles. Unlike commercial SPIONs, which often maximize their SAR and relaxivity values in an uncontrolled manner, our NPs are engineered to self-regulate their magnetic properties as a function of their temperature. This design prevents them from reaching excessively high temperatures that could potentially damage surrounding healthy tissues. Despite this self-regulation, our NPs maintain a sufficiently high SAR value, ensuring they remain effective for hyperthermia treatment. Future developments will prioritize strategies to optimize key physicochemical properties, such as NPs composition, size and size distribution,[34] to further enhance their performance. Our results also highlight the importance of surface coatings in evaluating biomedical applications. Further research will be dedicated to optimizing surface coatings to enhance stability, biocompatibility, and overall efficacy. For instance, modifying the PEG density and length could further reduce recognition by the RES and prolong blood circulation.[32] Additionally, exploring alternative or hybrid coatings, such as zwitterionic or stealth polymers, may further improve biocompatibility and reduce non-specific interactions. While intratumoral injection remains the primary approach for MFH, even in clinical settings, targeting NPs using magnetic fields presents a promising avenue for improving specificity and therapeutic efficacy, which warrants further investigation. Moreover, we aim to explore the combined imaging and hyperthermia treatment efficacy of M55 NPs in vivo to better understand their clinical potential.

Conclusion

This study highlights the potential of M55 NPs, coated with glucose (GM55), chitosan (CM55), and PEG (PM55), as promising theranostic agents for cancer treatment. The physicochemical characterization confirmed their stability and effective surface functionalization, with each coating imparting unique properties suited to different biomedical applications.

Our comprehensive in vitro evaluation demonstrated the biocompatibility of M55 NPs and their capability to efficiently act as mediators of MFH and as dual imaging CAs for MRI and MPI. The coatings significantly influenced cellular uptake, with certain variants better suited for applications like cell tracking and targeted hyperthermia therapy.

The dual-imaging capabilities of M55 NPs, combining the quantitative tracer detection of MPI with the high-resolution imaging of MRI, present a robust platform for non-invasive monitoring of NPs distribution and therapeutic response.

Overall, M55 NPs represent a versatile and practical approach for integrated cancer diagnostics and therapy. Future work will optimize NPs design, enhance circulation times, and conduct in vivo studies to explore their clinical potential and efficacy further.

Abbreviations

AMF, Alternating Magnetic Field; CA, Contrast Agent; CM55, Chitosan-coated M55 nanoparticle; DLS, Dynamic Light Scattering; DMEM, Dulbecco's Modified Eagle's Medium; DMSO, Dimethyl Sulfoxide; EPR, Enhanced Permeability and Retention; FT-IR, Fourier-Transform Infrared Spectroscopy; GM55, Glucose-coated M55 nanoparticle; ICP-OES, Inductively Coupled Plasma Optical Emission Spectroscopy; MFH, Magnetic Fluid Hyperthermia; MNPs, Magnetic

Nanoparticles; MPI, Magnetic Particle Imaging; MRI, Magnetic Resonance Imaging; MTT, 3-(4,5-Dimethylthiazol-2-yl)-2,5-Diphenyltetrazolium Bromide; NPs, Nanoparticles; PBS, Phosphate-Buffered Saline; PEG, Poly-ethylene Glycol; PM55, PEG-coated M55 nanoparticle; PSF, Point Spread Function; RES, Reticuloendothelial System; SNR, Signal-to-Noise Ratio; SPIONs, Superparamagnetic Iron Oxide Nanoparticles; SAR, Specific Absorption Rate; SRT, Self-Regulating Temperature; TEM, Transmission Electron Microscopy; XRPD, X-Ray Powder Diffraction.

Acknowledgment

MRI experiments were performed at the Centro Piattaforme Tecnologiche (CPT, University of Verona), with the technical help of Elena Nicolato, University of Verona, which is gratefully acknowledged.

The authors acknowledge the facilities and scientific support provided by the UNSW Sydney node of the National Imaging Facility (NIF) Australia and technical assistance by Dr Saeed Shanehsazzadeh and Brendan Lee at the Biological Resources Imaging Laboratory (BRIL), UNSW Sydney.

Funding

This research was supported by the AIRC Foundation, under IG 2022, ID. 27200, project PI: Pasquina Marzola. Financial support obtained from the Foundation for Nanotheranostics Research in Cancer Therapy, RNC (Treviso, Italy) is gratefully acknowledged. Prof. Adolfo Speghini and Dr Emil Milan acknowledge funding support from the PRIN-PNRR project, Mission 4 – Component 2 – Investment 1.1, funded by the European Union - Next Generation EU, project no. P2022XMF43 "OPTIMISE", and the Italian Ministry of University and Research (MUR), Italy. Prof. Adolfo Speghini acknowledges support by #NEXTGENERATIONEU (NGEU) and the Italian Ministry of University and Research, National Recovery and Resilience Plan (PNRR) under M4C2-I1.3, project MNESYS (PE0000006) "A Multiscale integrated approach to the study of the nervous system in health and disease" (DN. 1553 11.10.2022, CUP: B33C22001060002) and project HEAL ITALIA (PE00000019) "Health Extended ALliance for Innovative Therapies, Advanced Lab-research, and Integrated Approaches of Precision Medicine" (CUP: B33C22001030006).

Disclosure

The author(s) report no conflicts of interest in this work.

References

1. Kaur R, Bhardwaj A, Gupta S. Cancer treatment therapies: traditional to modern approaches to combat cancers. *Molecular Biology Reports*. 2023;50(11):9663–9676. doi:10.1007/s11033-023-08809-3
2. Arruebo M, Vilaboa N, Saez-Gutierrez B, et al. Assessment of the evolution of cancer treatment therapies. *Cancers*. 2011;3(3):3279–3330. doi:10.3390/cancers3033279
3. Lu Y, Rivera-Rodriguez A, Tay ZW, et al. Combining magnetic particle imaging and magnetic fluid hyperthermia for localized and image-guided treatment. *Int J Hyperthermia*. 2020;37(3):141–154. doi:10.1080/02656736.2020.1853252
4. Egea-Benavente D, Ovejero JG, Morales MDP, Barber DF. Understanding MNPs behaviour in response to AMF in biological milieus and the effects at the cellular level: implications for a rational design that drives magnetic hyperthermia therapy toward clinical implementation. *Cancers*. 2021;13(18):4583. doi:10.3390/cancers13184583
5. Dewhirst MW, Viglianti BL, Lora-Michiels M, Hanson M, Hoopes PJ. Basic principles of thermal dosimetry and thermal thresholds for tissue damage from hyperthermia. *Int J Hyperthermia*. 2003;19(3):267–294. doi:10.1080/0265673031000119006
6. Gerosa M, Grande MD, Busato A, et al. Nanoparticles exhibiting self-regulating temperature as innovative agents for magnetic fluid hyperthermia. *Nanotheranostics*. 2021;5(3):333–347. doi:10.7150/ntno.55695
7. Attaluri A, Kandala SK, Wabler M, et al. Magnetic nanoparticle hyperthermia enhances radiation therapy: a study in mouse models of human prostate cancer. *Int J Hyperthermia*. 2015;31(4):359–374. doi:10.3109/02656736.2015.1005178
8. Wust P, Hildebrandt B, Sreenivasa G, et al. Hyperthermia in combined treatment of cancer. *Lancet Oncol*. 2002;3(8):487–497. doi:10.1016/s1470-2045(02)00818-5
9. Tohnai I, Goto Y, Hayashi Y, Ueda M, Kobayashi T, Matsui M. Preoperative thermochemotherapy of oral cancer using magnetic induction hyperthermia (Implant Heating System: IHS). *Int J Hyperthermia*. 1996;12(1):37–47. doi:10.3109/02656739609023688
10. Elming PB, Sorensen BS, Oei AL, et al. Hyperthermia: the optimal treatment to overcome radiation resistant hypoxia. *Cancers*. 2019;11(1):60. doi:10.3390/cancers11010060
11. Dayanc BE, Beachy SH, Ostberg JR, Repasky EA. Dissecting the role of hyperthermia in natural killer cell mediated anti-tumor responses. *Int J Hyperthermia*. 2008;24(1):41–56. doi:10.1080/02656730701858297

12. Jasmin, de Souza GT, Louzada RA, Rosado-de-Castro PH, Mendez-Otero R, Campos de Carvalho AC, Carvalho ACC. Tracking stem cells with superparamagnetic iron oxide nanoparticles: perspectives and considerations. *Int J Nanomed*. 2017;12:779–793. doi:10.2147/ijn.S126530
13. Dias AMM, Courteau A, Bellaye P-S, et al. Superparamagnetic iron oxide nanoparticles for immunotherapy of cancers through macrophages and magnetic hyperthermia. *Pharmaceutics*. 2022;14(11):2388. doi:10.3390/pharmaceutics14112388
14. Kostevšek N. A review on the optimal design of magnetic nanoparticle-based T2 MRI contrast agents. *Magnetochemistry*. 2020;6(1):11. doi:10.3390/magnetochemistry6010011
15. Reichenbach JR, Schweser F, Serres B, Deistung A. Quantitative susceptibility mapping: concepts and applications. *Clin Neuroradiol*. 2015;25 (Suppl 2):225–230. doi:10.1007/s00062-015-0432-9
16. Gleich B, Weizenecker J. Tomographic imaging using the nonlinear response of magnetic particles. *Nature*. 2005;435(7046):1214–1217. doi:10.1038/nature03808
17. Goodwill PW, Conolly SM. The X-space formulation of the magnetic particle imaging process: 1-D signal, resolution, bandwidth, SNR, SAR, and magnetostimulation. *IEEE Trans Med Imaging*. 2010;29(11):1851–1859. doi:10.1109/TMI.2010.2052284
18. Saritas EU, Goodwill PW, Croft LR, et al. Magnetic particle imaging (MPI) for NMR and MRI researchers. *J Magn Reson*. 2013;229:116–126. doi:10.1016/j.jmr.2012.11.029
19. Matteazzi P, Gherlinzoni F, Gottardi M. inventors; method for the production of sub-micrometric particles and their theranostic use in oncology with specific apparatus. *Patent 2961429B1*. 2017.
20. Vurro F, Gerosa M, Busato A, et al. Doped ferrite nanoparticles exhibiting self-regulating temperature as magnetic fluid hyperthermia antitumoral agents, with diagnostic capability in magnetic resonance imaging and magnetic particle imaging. *Cancers*. 2022;14(20):5150. doi:10.3390/cancers14205150
21. Matteazzi P. Mechanomaking of nanophased materials. In: Rühle M, Gleiter H, editors. *Interface Controlled Materials*. Weinheim, Germany: Wiley-VCH Verlag GmbH & Co KGaA; 2005:118–125.
22. Chen X-G, Park H-J. Chemical characteristics of O-carboxymethyl chitosans related to the preparation conditions. *Carbohydr Polym*. 2003;53 (4):355–359. doi:10.1016/S0144-8617(03)00051-1
23. Boyer J-C, Manseau M-P, Murray JI, Van Veggel FC. Surface modification of upconverting NaYF4 nanoparticles with PEG− phosphate ligands for NIR (800 nm) biolabeling within the biological window. *Langmuir*. 2010;26(2):1157–1164. doi:10.1021/la902260j
24. Hergt R, Dutz S. Magnetic particle hyperthermia—biophysical limitations of a visionary tumour therapy. *J Magn Magn Mater*. 2007;311 (1):187–192. doi:10.1016/j.jmmm.2006.10.1156
25. Rose A. The sensitivity performance of the human eye on an absolute scale. *JOSA*. 1948;38(2):196–208. doi:10.1364/JOSA.38.000196
26. Gerosa M, Ren G, Zhang Y, et al. Preliminary results: imaging of in situ labeled tumor-associated macrophages with magnetic particle imaging. *Int J Magn Part Imaging IJMPI*. 2020;6(2 Suppl 1). doi:10.18416/IJMPI.2020.2009068
27. Colbert CM, Ming Z, Pogosyan A, Finn JP, Nguyen K-L. Comparison of three ultrasmall, superparamagnetic iron oxide nanoparticles for MRI at 3.0 T. *J Magn Reson Imaging*. 2023;57(6):1819–1829. doi:10.1002/jmri.28457
28. Wang Y-XJ. Superparamagnetic iron oxide based MRI contrast agents: current status of clinical application. *Quant Imaging Med Surg*. 2011;1 (1):35–40. doi:10.3978/j.issn.2223-4292.2011.08.03
29. Williams R, Sehl O, Gevaert J, et al. Dual magnetic particle imaging and akaluc bioluminescence. *Tomography*. 2023;9(1):178–194. doi:10.3390/tomography9010016
30. Hasnain MS, Nayak AK. 21 - Chitosan as responsive polymer for drug delivery applications. *Stimuli Responsive Polymeric Nanocarrier Drug Delivery App*. 2018;581–605.
31. Graván P, Peña-Martín J, de Andrés JL, et al. Exploring the impact of nanoparticle stealth coatings in cancer models: from PEGylation to cell membrane-coating nanotechnology. *ACS Appl Mater Interfaces*. 2024;16(2):2058–2074. doi:10.1021/acsami.3c13948
32. Shi L, Zhang J, Zhao M, et al. Effects of polyethylene glycol on the surface of nanoparticles for targeted drug delivery. 10.1039/D1NR02065J. *Nanoscale*. 2021;13(24):10748–10764. doi:10.1039/D1NR02065J
33. Ota S, Trisnanto SB, Takeuchi S, Wu J, Cheng Y, Takemura Y. Quantitation method of loss powers using commercial magnetic nanoparticles based on superparamagnetic behavior influenced by anisotropy for hyperthermia. *J Magn Magn Mater*. 2021;538:168313. doi:10.1016/j.jmmm.2021.168313
34. Dadfar SM, Camozzi D, Darguzyte M, et al. Size-isolation of superparamagnetic iron oxide nanoparticles improves MRI, MPI and hyperthermia performance. *J Nanobiotechnol*. 2020;18(1):22. doi:10.1186/s12951-020-0580-1